NPL
National Physical Laboratory

NPL REPORT MAT 128

UNCERTAINTIES OF IN SITU MICROMECHANICAL TESTING OF ADDITIVE LAYER MANUFACTURING (ALM) MATERIALS

A KOKO, A T FRY, K MINGARD

MARCH 2024

Uncertainties of in situ micromechanical testing of additive layer manufacturing (ALM) materials

A Koko, A T Fry, K Mingard
Advanced Engineered Materials

ABSTRACT

The report investigates uncertainties in in-situ micromechanical testing of additive layer manufacturing (ALM) materials within a scanning electron microscopy (SEM) framework. It identifies displacement and load measurements, and sample alignment as the primary uncertainty sources. By addressing these uncertainties, offering mitigation strategies, and advancing material design and manufacturing processes, the study aims to enhance mechanical property evaluations' accuracy and reliability in ALM materials.

ISSN: 1754-2979

DOI ADDRESS: https://doi.org/10.47120/npl.MAT128

National Physical Laboratory
Hampton Road, Teddington, Middlesex, TW11 0LW

This work was funded by the UK Government's Department for Science, Innovation & Technology through the UK's National Measurement System programmes.

Approved on behalf of NPLML by
Stefanos Giannis, Science Area Leader.

CONTENTS

1 INTRODUCTION

In-situ micromechanical testing within the scanning electron microscope (SEM) offers insight into the mechanical properties of Additive Layer Manufacturing (ALM) materials. This technique allows researchers to observe and measure the behaviours of materials under load in real-time, providing critical data for understanding the factors controlling deformation and fracture. However, the precision and reliability of these measurements are subject to various sources of uncertainties that can significantly impact the outcomes of the tests [1–3].

The primary sources of uncertainties in *in-situ* micromechanical testing arise from displacement and load measurements, sample alignment, and the inherent limitations of the SEM environment. Displacement and load measurements are crucial for determining the mechanical properties of materials, such as Young's modulus, yield strength, and ultimate tensile strength. However, the accuracy of these measurements can be compromised by the resolution and calibration of the SEM's micromechanical stage, as well as the precision of the force sensors and displacement actuators used in the setup.

Sample alignment presents another critical source of uncertainty. Proper sample alignment is essential for applying loads uniformly and ensuring that measurements reflect the intrinsic properties of the material rather than artefacts of misalignment. Misalignment can lead to non-uniform stress distributions, affecting the accuracy of critical measurements like strain and stress fields within the material, and affect mechanical properties such as modulus, maximum elongation, and tensile strength [4].

Moreover, the SEM environment itself introduces additional challenges. Factors such as electron beam interactions with the sample can lead to charging effects or localised heating, potentially altering the material's properties during the test. These effects must be carefully managed and accounted for to ensure the accuracy of the test results.

Despite these challenges, in-situ micromechanical testing remains a powerful tool for understanding the mechanical behaviours of ALM materials. By identifying and addressing the sources of uncertainties, researchers can enhance the reliability of their measurements and

advance the development of materials with optimised mechanical properties for a wide range of applications.

This report considers the factors affecting the accuracy of results from in-situ micromechanical testing of additive layer manufacturing (ALM) materials. Results of testing fine scale lattice structures that ALM makes feasible are shown to illustrate sources of uncertainty. Specifically, it will focus on the uncertainties related to displacement and load measurement, and sample alignment, but not the effects of the SEM environment.

2 METHODOLOGY

2.1 SAMPLES DESIGN AND MANUFACTURING

The primary focus was on creating specimens that allow for the tensile testing of individual lattice/ligament elements, a deviation from the conventional testing of larger, multi-cellular lattice configurations commonly reported in the literature. The design process utilised an open-source parametric CAD program, OpenSCAD to generate a surface tessellation model (STL) file suitable for 3D printing. Special attention was given to accurately rendering the smooth curves of the gauge sections and tapers, ensuring the physical models' fidelity to the designed parameters. More details can be found in A. Fry et al. [5,6].

A novel aspect of the specimen design was the integration of a cassette system to enhance the manufacturability and handling of the test pieces. The cassette allowed for multiple specimens to be produced and maintained together in a spur-type configuration, encased on all sides by a solid wall, except for strategically placed holes for post-manufacture processing. This design facilitated easier handling, transport, and identification of individual specimens, demonstrating an innovative approach to specimen management in the context of tensile testing.

Furthermore, the specimens were designed to be compatible with a broad spectrum of testing equipment without necessitating custom mounts or grips. The grip sections of the test pieces were crafted to accommodate both wedge action grips, commonly found in universal test systems, and simple plate systems secured with bolts, typically used in smaller-scale sample testing. This versatility ensured that the test specimens could be readily integrated into existing

testing frameworks, thereby expanding their applicability and ease of use in research environments.

The specimens were constructed from AlSi10Mg powder using a laser powder bed manufacturing technique, a method well-suited for producing detailed and precise geometries required for the study. The main test piece is protected from accidental or premature damage by side supports (Figure 1a).

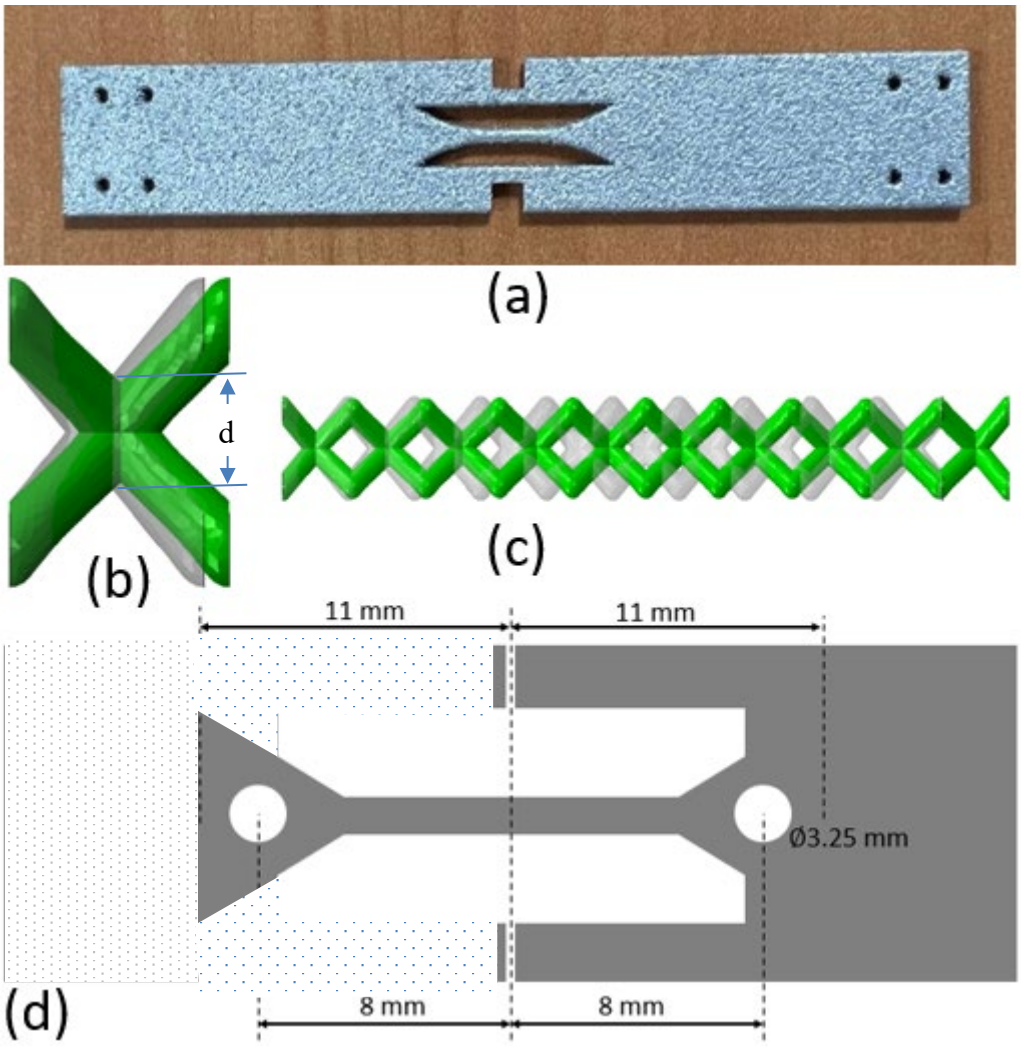

Figure 1: (a) As received single ligament test specimen manufactured from AlSi10Mg. (b) Schematic of a single unit cell of a multi-ligament lattice structure. (c) 1 node wide lattice sample (d) Schematic for a signal ligament of the sample with the left hand side showing the final sample shape after machining to suit the dowel pin loading employed.

The tested samples were either single 0.5 mm and 0.75 mm diameter single ligament samples (Figure 1a), or multi-ligament lattice structures with 1, 2 or 5 nodes, all with a 0.5 mm effective single unit cell diameter. The effective single unit-cell (or node) diameter was measured at the centre of Figure 1b. To allow for mechanical testing inside the SEM, the specimen (Figure 1a) was further machined to remove the side supports, shorten the length of the sample to 22mm, and drill two 3.25 mm diameter holes at each end of the test specimen to allow the sample (Figure 1d) to be fitted and tested using a single leadscrew 2kN Deben MT2000EH rig to perform mechanical testing at room temperatures inside the Thermo Fisher Apreo SEM, as shown in Figure 2. From SEM images, it can be observed that there are surface asperities on the gauge length.

2.2 MICROMECHANICAL TESTING

The tensile tests were conducted using a single leadscrew Deben MT2000EH test rig. This rig is a tensile, compression and horizontal bending stage designed for real-time observation of high-stress regions of a sample with an SEM, optical microscope, AFM, or XRD system. It uses a miniature 2kN load cell. Samples are mounted horizontally, and supported on stainless steel slide bearings before being tested in tension.

To ensure accurate measurements, the supplier calibrated the 2 kN load cell before delivery. Additionally, a 10.03 mm x 15.13 mm displacement setup block was used to set the rig's zero displacement value by closing the jaws until the setup block fits between them. The block was clamped between the jaws using the software, ensuring approximately 5-10N of compression force was shown on the readout.

The test pieces were gripped using a pair of 3.25-diameter rods (Figure 2b) to minimise the difficulties of clamping the small test pieces and avoid slipping. These rods are made of tool steel, which is especially hard and resists abrasion and wear.

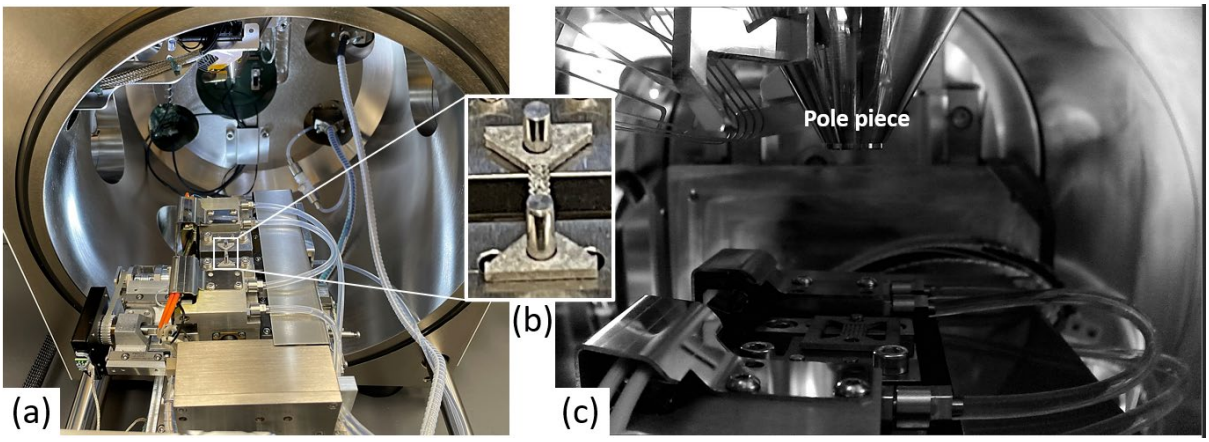

Figure 2: (a) Deben MT2000EH rig after being fitted to the Thermo Fisher Apreo SEM's sample holder. (b) A close-up of a single unit cell sample fixed on the rig by 3.25 mm diameter rods. (c) The Deben rig inside the SEM is under vacuum at room temperature, with the sample being observed using secondary electrons.

The test pieces were loaded at a crosshead speed of 0.1 or 0.2 mm per minute and deformed in tension. This speed is set to ensure a consistent extension rate during the test, which is essential for achieving accurate and consistent results.

During testing, the sample was imaged using the secondary electron (SE) at 10 kV and 1 nA beam conditions. Non-contact strain measurement solutions were used to capture multi-axis displacements from which strain and strain rates could be calculated. The images were used over large fields of view to measure the strain over the whole gauge length, or on multiple discrete areas to simulate a standard strain gauge measurement, or markers can be used combined with an image correlation extensometer approach. Figure 4 (without loading) and Figure 5 (with loading) show examples of the captured images.

2.3 IMAGE TRACKING

During these tests, 1536 × 1024-pixel SEM images were collected to quantify the stage displacement accuracy. This was done both without loading being applied and while loading was applied. The purpose of this was to gauge the effect of compliance and sample traction on the rig measurement of displacement. The alignment and calibration of the test machine and grips, as well as the loading at a specific crosshead speed, are all critical factors that can influence these measurements. Using the SEM images in conjunction with the Linear Stack

Alignment with the Scale Invariant Feature Transform (SIFT) plugin in Fiji ImageJ makes it possible to accurately align the image stacks and thereby enhance the precision of the stage displacement measurements. The SIFT algorithm identifies scale-invariant features in an image and uses them to locate an object in an image [7]. The plugin works by first converting the images to stacks; then, the function is run to extract the SIFT correspondences and determine the movement in the X and Y-axis between the images, using the SEM dimensional calibration to convert movement in pixels to micrometres.

One of the challenges with this plugin is that it uses the entire image for feature extraction, which can lead to increased alignment error if certain regions of the image are irrelevant for the alignment. To address this, we have made the plugin work with a Region of Interest (ROI), ensuring that feature extraction is only applied to a specific region within the stack. The movement tracking measurement was then applied across different ROIs and images to quantify the stage displacement accuracy.

3 RESULTS AND DISCUSSION

3.1 DISPLACEMENT MEASUREMENT

3.1.1 Displacement sensing

In Figure 3a, the red curve plots the force (right hand Y -axis) against the displacement recorded by the system extensometer. It also plots in black on the left Y-axis the difference between the extensometer values and the expected displacement based on the programmed displacement rate (0.1 mm/min or 0.2 mm/min). In general, the differences were small and within the limits of the resolution of the measurement systems. Where the differences were larger the points are indicated by blue shaded lines. All the shaded points correlate very well with changes in the applied loading rate, from when the sample started to experience load and fracture in each of the unit cell's four joints.

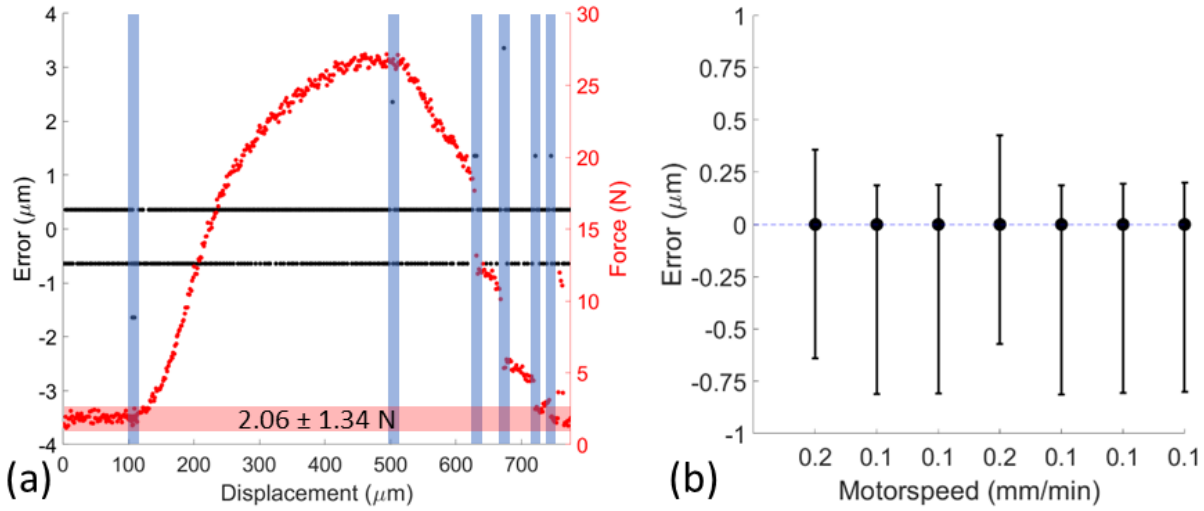

Figure 3: (a) Irregularities (or errors) in the recorded stage movement for an ALM sample with 1 unit cells, calculated from the difference between consecutive elongation values minus the calculated strain rate. The irregularities in applied displacement were plotted with the sample force on the second Y-axis of the plot. (b) The absolute error was recorded in different tests that were conducted using different strain rates.

The mean and range of the absolute differences in elongation (after removing outliers) calculated across different tests was then plotted in Figure 3b, which shows that difference was greater at the slower rate of 0.1 mm/min with a typical range of -0.75 µm/+0.25 µm. At 0.2 mm/min the range was closer to ± 0.5 µm. Therefore, the stage control at low loads of displacement – as recorded by the stage instrument – is remarkably consistent unless there is an abrupt change in force.

3.1.2 Without loading

While imaging a broken half of a test sample, the rig was moved by specific distances without, therefore, a load being applied. The SEM's field of view was focused so that features were imaged before and after the stage was displaced by a specific value. A MATLAB code written to analyse and visualise the tracked movement in a set of images obtained during the test and using the Linear Stack Alignment with SIFT plugin in Fiji (ImageJ). The code starts by defining arrays to store the number of features extracted from each image set (Figure 4d), the original images, subsequent images at different stage movements, the recorded displacement of the stage, and transformation matrices from the SIFT algorithm that include rotation, scaling, and

translation parameters for each set of images. Using the pixel size, the absolute values of translation parameters (from the matrices) were converted into micrometres.

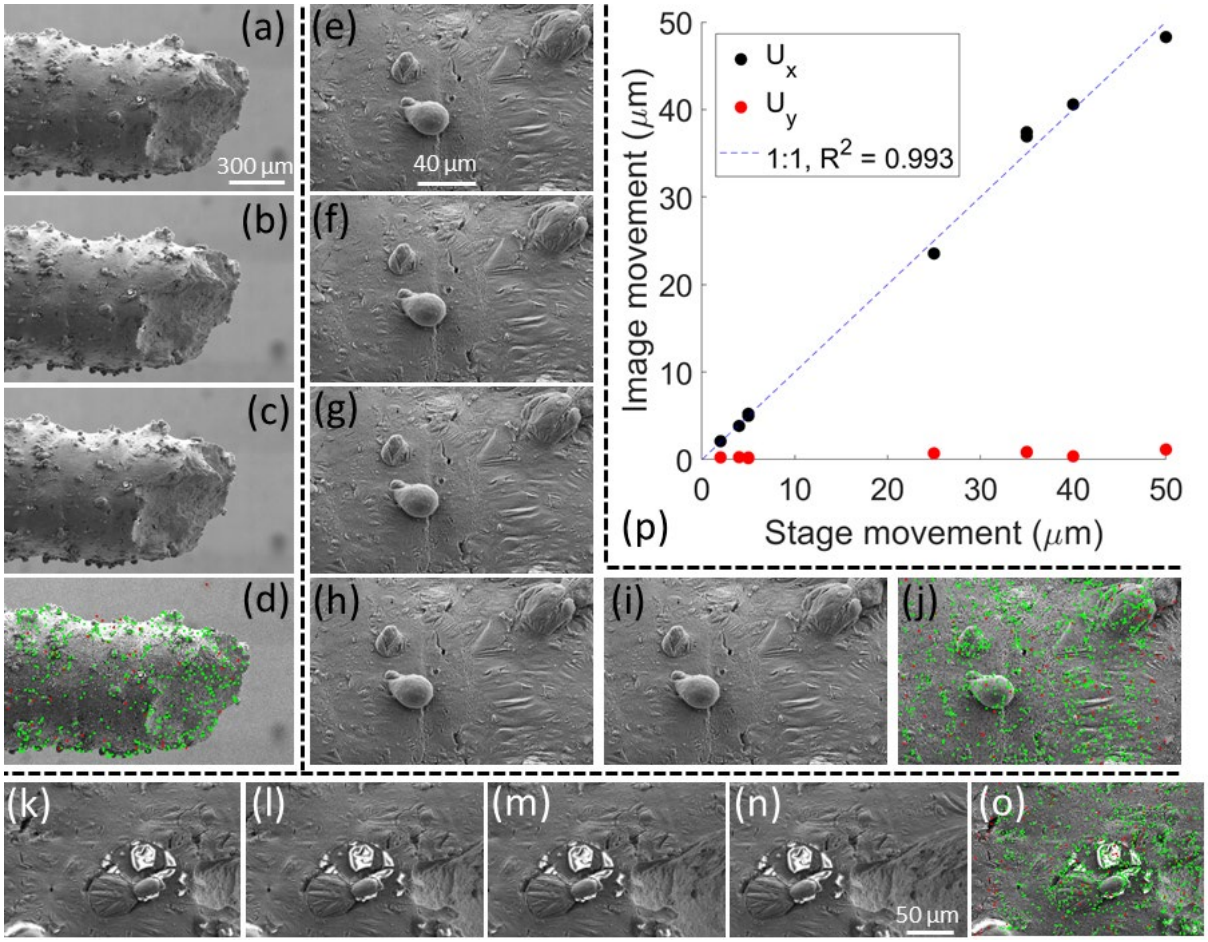

Figure 4: Three different 1536 x 1024-pixel fields of view (a to c, e to i, and k to n) that were moved from the original position. The features in d, j and o were tracked across the three FOVs, compared to the recorded jaw displacement, and plotted in (p).

Figure 4a to c show the unloaded sample being moved in the X-axis by 50 µm and 75 µm with a pixel size of 1 µm for each image. Smaller steps were used for the two fields of view (FOV) shown in Figure 4e to i and k to n, in which the distances moved were 2, 7, 11, 16 µm, and 40, 75 and 110 µm, respectively, from the original position. The two FOV had pixel widths of 127 and 254, respectively. More than 2000 features being extracted and tracked in each of the 3 different FOVs (Figure 4d, j and o).

The calculated image movements were plotted against the recorded stage movements, and two separate plots were created for horizontal (X-axis) and vertical (Y-axis) displacements (Figure

4p). This visualisation helps in understanding how much the FOVs have moved compared to the physical movement of the stage. The plotted data was then fitted using a linear least squares fitting, aiming to find a relationship between the stage movement and the image movement. We used robust fitting methods to improve the accuracy of the fit. The goodness of fit is evaluated and displayed in the plot legend, indicating how well the calculated displacements match the actual stage movements. Figure 4p shows a good agreement between the stage movement and calculated image movement. There is a minimal (<1 μm) Y-axis movement that might be due to the beam deflection/image drift during image acquisition and can be neglected considering the FOVs' pixel size. Therefore, in the absence of loading, the recorded stage movement is accurate.

3.1.3 With loading - the effect of compliance

The Deben rig was used to deform a range of ALM samples but the following uses specific measurements on a two unit-cell sample tested at 0.1 mm/min strain rate while the SEM image field of view was focused on a part of the moving jaw (Figure 5a). The movement in the field of view was tracked at a rate of 0.5 s/image, and the Linear Stack Alignment with SIFT used to track more than 1000 features. The tracked movements were compared against the recorded stage displacement, recorded at the same rate (Figure 5b). However, after closely examining the acquired images' time stamp, it was found that the acquisition rate fluctuated. Thus, the images' actual time stamp was used to correctly match the data and image timestamps, with minimal cubic interpolation needed to complete the match between the two datasets. Then, the difference between the two was plotted as the error in Figure 5c and d, and visualised against the force, recorded during the test to visualise how the error changed depending on the sample behaviour under load.

In the initial phase, the recorded stage displacement agreed with the measurements from the images until the sample began to be loaded at point 1. Following this, the stage-applied displacement (as measured from the images) and the stage's recorded displacement began to diverge linearly, with the recorded error between measurement points being 0.23 μm/s and the gradient of the linear cumulative error equalling ≈0.8 μm/N until it reached a maximum stress of 53 N.

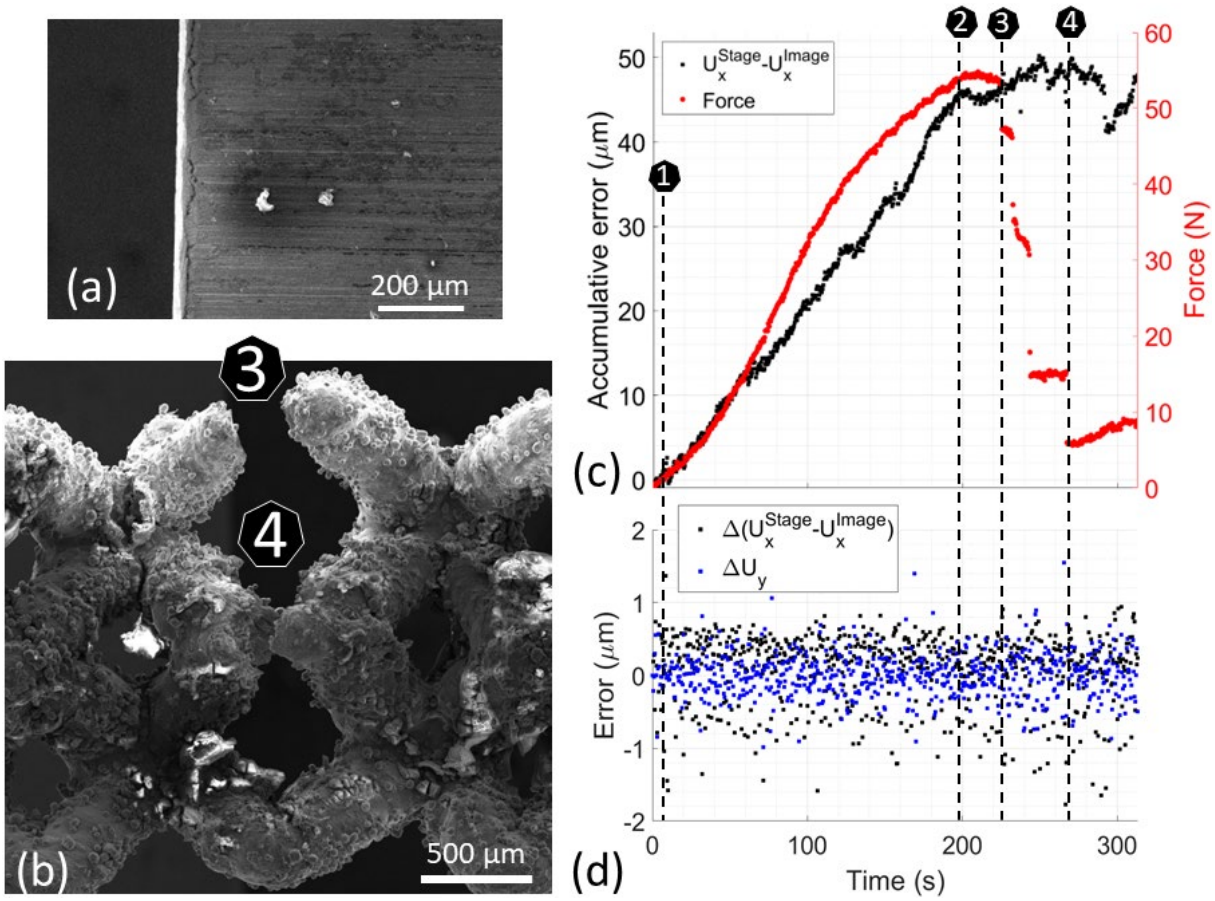

Figure 5: (a) The tracked 1536 x 1024-pixel field of view (FOV) at the moving jaw of the single leadscrew 2kN Deben rig while deforming an ALM sample with two unit cells. (b) Fractgorpahy of the sample with two unit-cells after the test. The difference between the measured FOV movement and the recorded jaw displacement was reported as (c) cumulative error and (d) data acquisition-dependent error. The data was acquired at a rate of 500 ms. The second red Y-axis in (c) also shows the force the ALM sample experienced during the 0.1 mm/s displacement control test.

Once the sample reached the UTS of the strain-stress curve (point 2), the applied and measured displacement remained relatively constant. There were some small changes in the difference between sample and jaw displacement from this point onwards, but these were relatively small.

By contrast, the difference between the Y-axis measurements did not accumulate and was around ± 0.25 µm, less than the image pixel size of 689 nm; thus, it can be considered due to noise.

3.1.4 General discussion

In general, the stage movement without load is accurate; however, when the load is applied, the expected stage movement measured by the rig software can exceed the actual movement measured from images of the sample or stage. This is a result of machine compliance. In the context of tensile testing, compliance refers to the deformation of the entire system – including the frame, load cell, grips, couplings, and specimen – when a force is applied. This deformation is not limited to the test specimen alone [8]. This means that the measured displacement is the sum of total system deformation. To determine the displacement of the specimen only, machine compliance (deformations associated with the load frame, load cell, and grips) must be removed from this measurement.

In our observations, while the stage displacement includes the deformation of the entire system, the displacement measured from the images likely represents the deformation of the specimen only. The effect of machine compliance may not be noticeable in the machine structure; however, it may significantly affect the tensile response result, leading to inaccurate reporting on the mechanical properties of tested materials. Therefore, it is essential to correct for machine compliance to obtain accurate displacement measurements. This can be done by subtracting the contribution due to the compliance of the loading train from the measured displacement. This correction can be particularly significant when the total displacement is small, as machine compliance can constitute a substantial portion of the output displacement.

The tests described here had a compliance (or error between measured and actual displacement) of about 0.8 μm/N. Repeated tests gave similar results. However, a significant fraction of this compliance may have arisen from the method of fixing the sample to the rig by dowel pins, as shown in Figure 2b. Further tests were carried out on a very large stainless steel test piece 25 mm wide by 2 mm thick which was effectively infinitely stiff, and the results shown in Figure 6. Note that this plots load against time: within this time period the total extension measured by the rig was less than 1 μm for each loading, so the compliance of the system must be less than 0.001 μm/N. However, in three of the tests plotted, load on the sample was only enabled by locating it over two dowels pushed into the rig jaws and for these three runs, the rate of loading started slowly and only increased to a constant rate after a significant fraction of the loading cycle had been completed. Below 100 N, the rate of increase was very slow in

comparison with the steady state. In contrast, the sample that was fully clamped between roughened jaws achieved a greater steady rate and achieved this rate much more quickly. While this is only based on load against time because the displacement was smaller than could be measured by the rig, it would seem likely that this behaviour would be mirrored in the load-displacement curves measured for less stiff samples and indeed Figure 7 and Figure 8 both show wide variations in the initial slopes of the load-displacement curves.

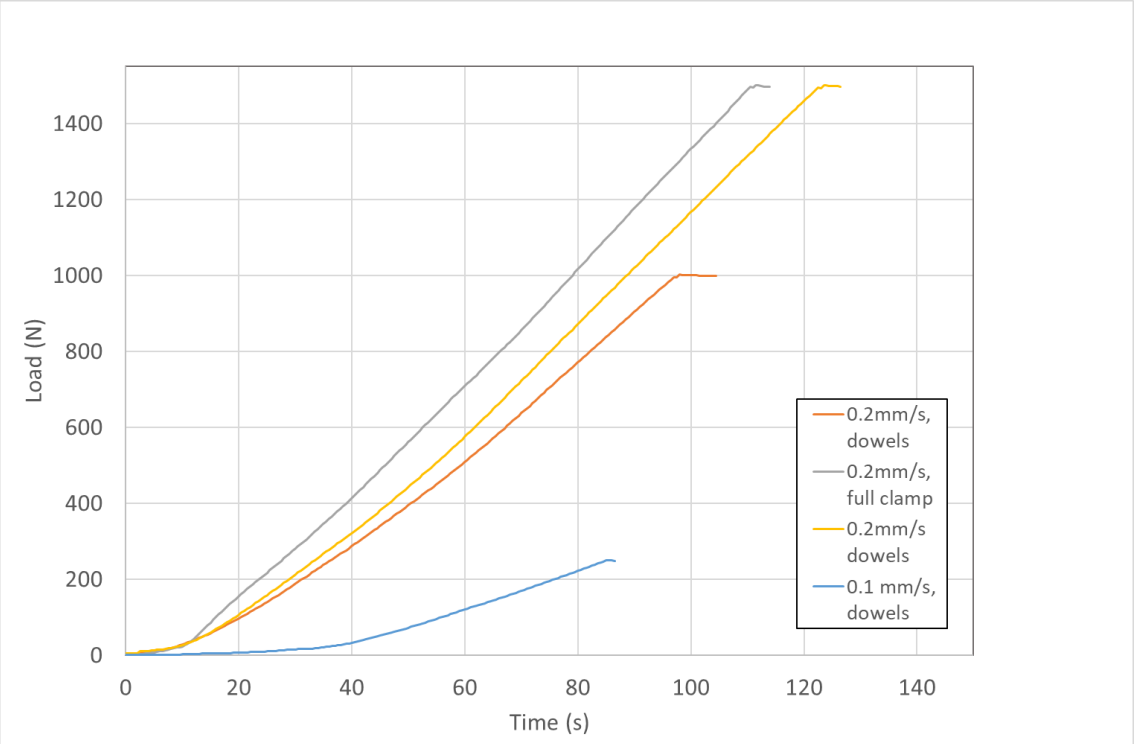

Figure 6. Load against time plots for an effectively infinitely stiff sample. Two different loading rates were used and results shown for loading the sample either fully clamped, or just located between two dowel pins on each side.

A full-field approach can be used to measure the strain over the whole gauge length, or multiple discrete areas can be selected, especially when heterogenous straining is expected, as shown in Figure 5. This allows the user to simulate a standard strain gauge measurement. Markers combined with an image correlation extensometer approach can also be employed to record the accurate displacement.

3.2 STRESS MEASUREMENT

3.2.1 Load measurement

To ensure accurate measurements, the supplier calibrated the 2 kN load cell before delivery. The calibration process involves converting the load cell signal into engineering units, which is often the most accurate method for measurement. However, preload force, also known as the phantom force, was determined to be approximately 2.1 ± 1.3 N, based on an average of eight tests.

The force versus displacement (or elongation) curves, obtained from testing various ALM lattice and single ligament samples within the SEM, are depicted in Figure 7a. These curves were adjusted by deducting the displacement at the preload point from the recorded displacement. The single ligament samples displayed typical stress-strain curves for AlSi10Mg prior to fracturing. The ALM sample composed of five-unit cells endured the highest force before fracturing. The test was paused at points 1 and 2 in Figure 7a to capture images of the entire sample. During this imaging process, a significant force relaxation was observed. The sample was subsequently loaded until it fractured, which happened across multiple unit cells, leading to a decrease in the load.

In the case of the ALM sample with two-unit cells, the sample began to fracture in stages. The first stage (point 3) occurred when the initial joint cracked, causing the load to decrease and be sustained by the unfractured portion of the sample. The deformation then proceeded with a gradual fracture at the weakest joint links at points 4 and 5, accompanied by a noticeable drop in force. A similar pattern was observed for the sample with a single unit cell at points 6 and 7.

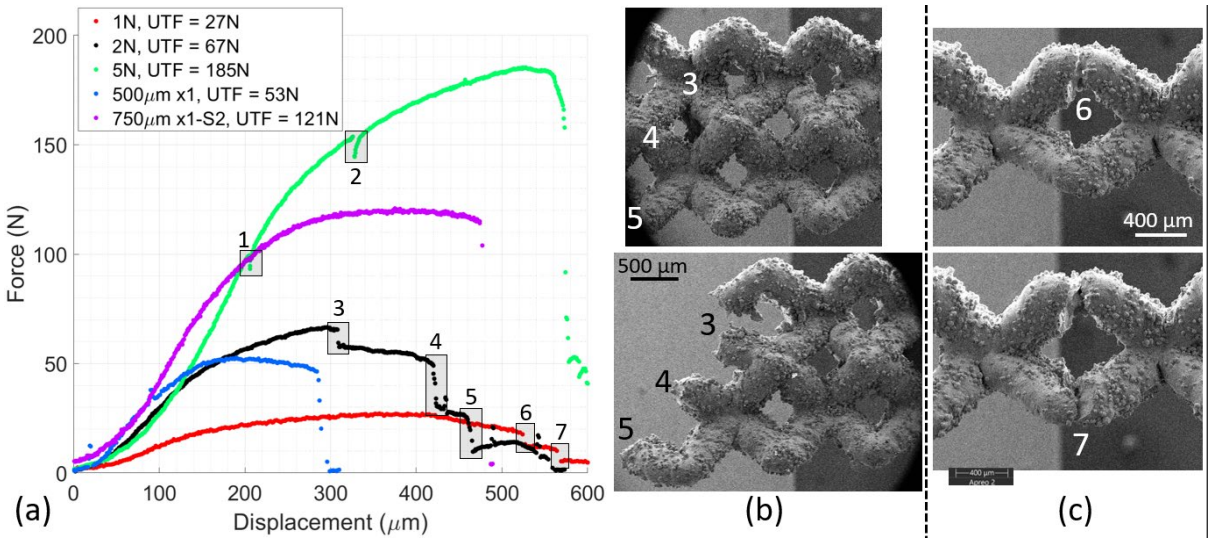

Figure 7: (a) Force vs displacement plots of ALM samples with 1, 2, and 5 unit-cells (labelled 1N, 2N, and 5N, respectively) and single ligament structures with 0.5 mm and 0.75 mm diameters. The legend shows the ultimate tensile force (UTF), which is the maximum applied force. (b) and (c) shows two and single unit-cell structures fractography as enumerated in (a).

3.2.2 Calculated stress

Using the nominal sample cross-section dimensions, the stress and strain curve were calculated and plotted in Figure 8, with the ultimate tensile stress (UTS) for each sample noted in the legend against each plot. The UTS appears to increase with the number of unit cells for the lattice samples but was consistent for the two different diameter single ligament samples. For the single ligament ALM sample with a 0.75 mm diameter, the test was repeated three times to see if there was consistency in the sample's mechanical properties.

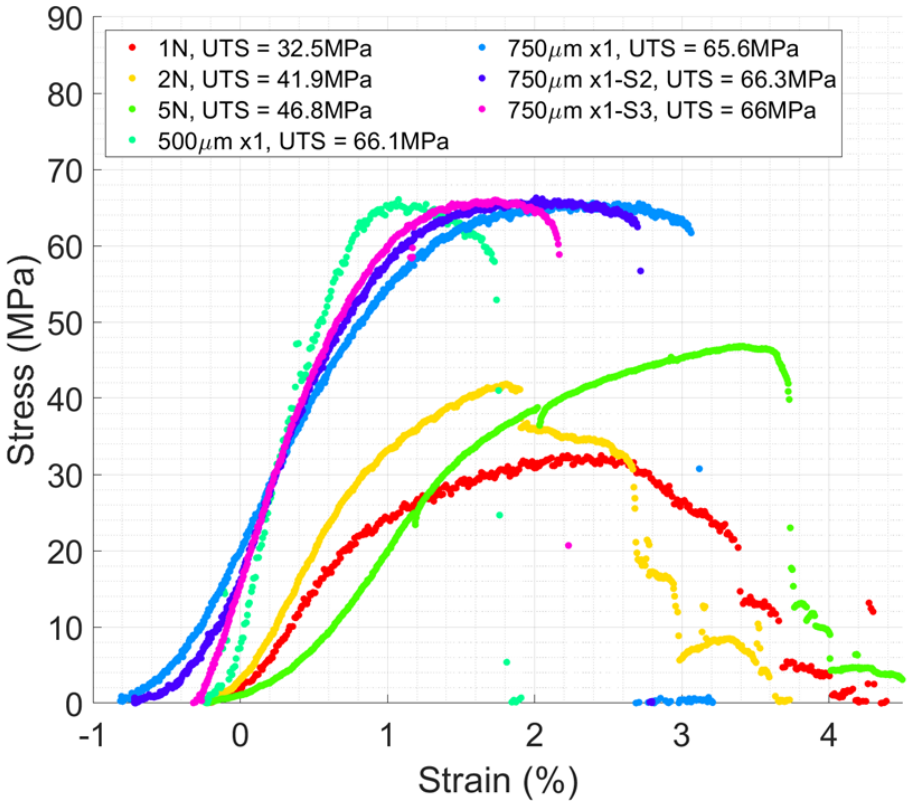

Figure 8: Stress-strain curves for the ALM samples.

Examination of the SEM images of the individual lattice samples showed a wide variation in sample diameters at different points. Multiple surface asperities from powder particles welded to the surface were present within the gauge length of the samples increased the difficulty of obtaining accurate measurements of the diameters. When these measurements were taken optically, it was found that the minimum diameter varied by as much as 70 µm. This variation introduces a significant level of uncertainty into the stress measurement calculations, estimated to be around 14%.

The complexity of this issue is further highlighted when considering the X-ray Computed Tomography (XCT) images of a single node sample, as shown in Figure 9. The XCT images reveal the intrinsic heterogeneity present during the ALM build process including the nonuniform cross-section and the presence of internal porosity. The large individual pores can reduce the sample cross section and potentially act as stress concentrators, but stress concentrations also occur at the nodes where the ligaments merge and where ligament directions changes. All these factors can lead to a reduction in the reported UTS if it is based on a nominal

diameter. In contrast the single ligament samples had a much more consistent diameter and this is reflected in the very similar measurements of UTS.

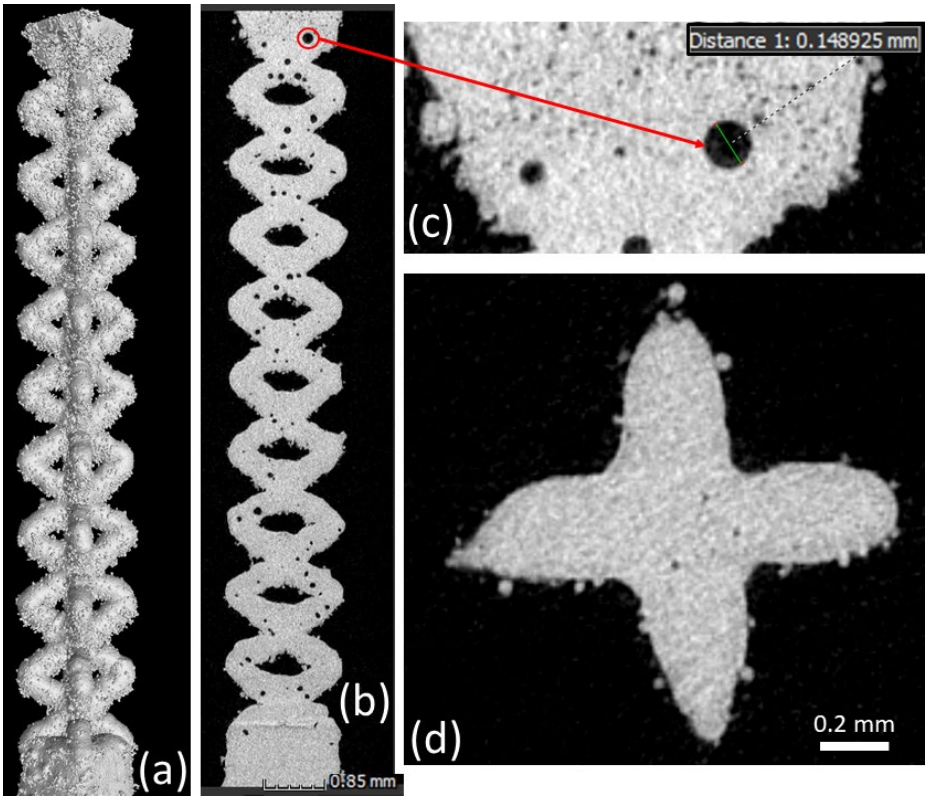

Figure 9: (a) X-ray Computed Tomography (XCT) scan for a single node ALM sample . (b) A 2D slice of the scan with (c) a zoom on a ~0.15 mm porosity and (d) one of the 3D nodes.

It is noteworthy that the stretch at the image's top is considerably smaller than that at the centre and bottom. This aligns with the fracture initiation near the top right of the sample, a region that consequently experiences reduced forces and less elongation early in the complete sequence.

3.2.3 Effect of stress relaxation

While testing the 5 unit-cells sample, the test was interrupted to image the entire sample. This caused load relaxation by approximately 10 N (~2 MPa), as seen in **Figure 6**a, points 1 and 2.

Generally, in metallic materials, stress relaxation can significantly alter the mechanical behaviour of the material [9]. Specifically, in aluminium alloys, stress relaxation aging (SRA) behaviour and its dependence on stress and temperature have been studied [10]. The apparent

activation energy of the material remains constant in the elastic region but decreases with the increase in strain in the plastic region, and also decreases with the increase in temperature for all initial loading stresses [10]. These characteristics contribute to a much higher degree of stress relaxation in the plastic region and at higher temperatures than in the elastic region and/or at lower temperatures [10].

Moreover, the initial stress can have a significant effect on stress relaxation, especially in the early stage of stress relaxation [11]. Larger initial stresses will produce large lattice spacing, and the diffusion rate of atoms will increase, resulting in easy dislocation movement and promoting stress relaxation [11].

3.2.4 General discussion

The accuracy of a load cell is usually expressed as a percentage of the full-scale output or reading. In the current case, the load cell supplied was certified with an accuracy of ±0.1% full-scale.

The repeated tests on similar samples yielding similar UTS values shown in Figure 8 provides a measure of the precision only of the load cell but not of the accuracy. Given that other factors such as sample homogeneity could affect the precision, it is perhaps surprising how consistent the results are for the ligament samples.

Bearing in mind this potential for variation between samples, which increases when the multi node samples are also tested, a further way of validating the accuracy of the miniature rig is to compare the results with those obtained on samples from the same batch tested on another rig. Figure 10 shows such a comparison in which the load displacement curves from the Deben miniature rig were compared with results obtained using an Instron 5969 universal mechanical test machine fitted with a 50 kN load cell. From Figure 10, the agreement is good, with similar load peaks differing by only ± 0.8 N for the samples with 5 and 2 unit cells. For the sample with a single unit cell, the discrepancies between the two rigs is larger with a difference of approximately 4.6 ± 2.2 N.

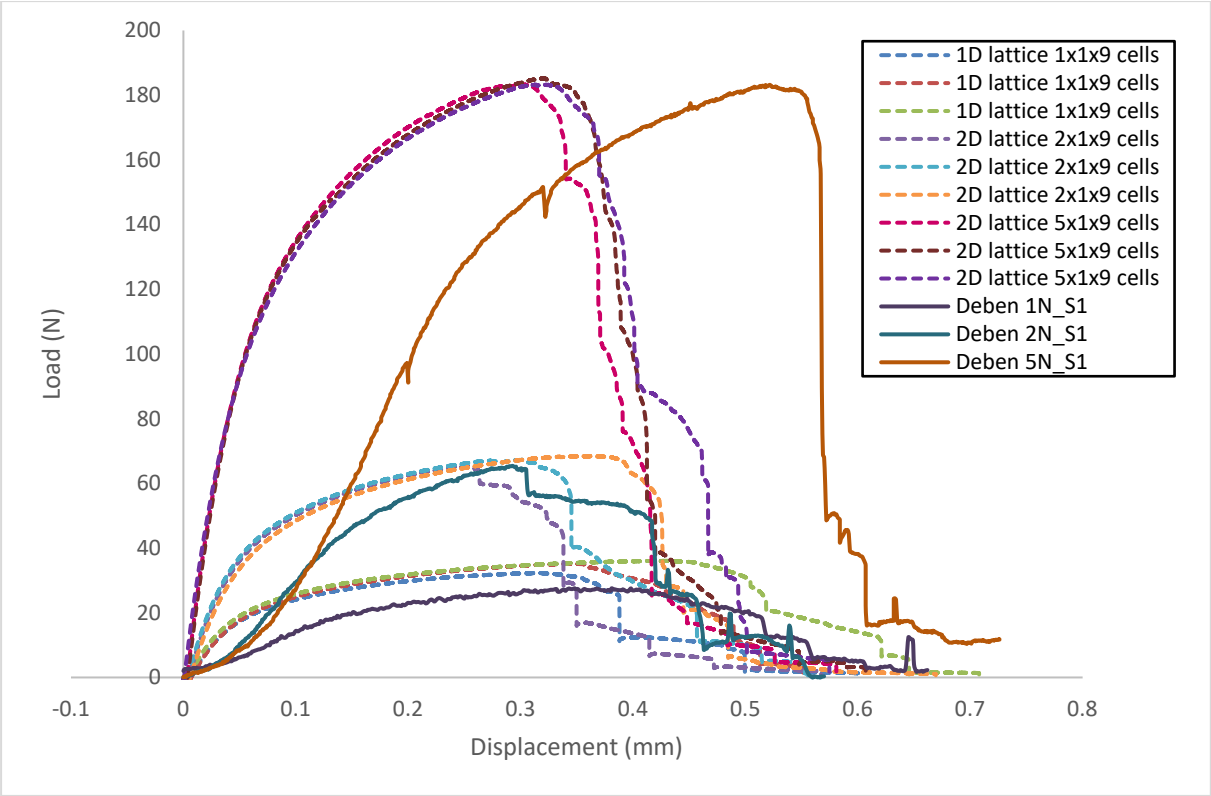

Figure 10: Stress-strain curves for the ALM unit-cell samples from the Deben rig and the Instron test frame.

However, it is also clear that there is a significant difference between results from the two rigs when the initial loading curves are compared. In contrast to the Instron results, the Deben rigs show a much greater lead in before the load began to increase rapidly, suggesting a greater elongation. However if this behaviour is compared with the results shown in Figure 6 then it is probable that the long lead of the Deben curves arises from the use of dowel pins to load the samples, rather than the clamping between jaws used with the Instron data. The lead in effect shown in Figure 6 is noticeable below 50 N, which is greater than the maximum load experienced for the single cell lattice samples.

Although the differences in maximum load between the 1, 2 and 5 node samples seen in Figure 10 are to be expected, the stress-strain curves in Figure 8 might also be expected to show similar UTS, but clearly UTS increases with the number of nodes. This is probably a consequence of the increase in number of ligaments averaging out the effects of individual defects (primarily porosity, stress concentrations, ligament diameters).

The plots of load against displacement for the 2 node sample in Figure 10 and Figure 7 show, for the in situ rig, the force rising in an “S” shaped curve: the rate of loading increases over the first 50 μm displacement to about 10 N, followed by a short linear region between 10 N and somewhere between ≈30 and 40 N (100 - 125 μm displacement). In contrast the sample in the Instron rig showed a rapid, steady rise to 40 N over only 50 μm displacement.

The Deben rig data was acquired simultaneously with imaging of the field of view shown below in Figure 11 using a fast scan rate to save a new image every 5 s. After alignment of the images with the SIFT algorithm, individual features (discrete powder particles on the sample surface) were manually identified in each image and the Fiji Trackmate plugin used to track the feature movements. The features were chosen to give pairs of points approximately 2 mm apart on the top, middle and bottom nodes (i.e. top, middle, and bottom of the image): the change in separation of these pairs was calculated to determine the % elongation over this 2 mm gauge length.

The three measurements of % elongation are plotted against time in Figure 13, along with the corresponding displacement measured by the rig transducer. Because starting of the image acquisition and of the loading on the rig was not linked and required individual manual initiation, there was some uncertainty in fixing a common start time for the elongation dataset and that of the rig displacement. The manual identification of features also added to the uncertainty in elongation. However, the overall picture is clear: the rig measured an almost linear increase in displacement, but the measured sample elongation was very small for approximately the first 100 s before rising quickly during plastic deformation to a plateau. The rig displacement in the first 100 s corresponds closely with the slow initial increase in load and linear rise to 30-40 N noted above. It suggests that the initial elastic deformation measured by the Instron rig was obscured in the in situ rig by, presumably, the bedding in of the sample on the dowel pins.

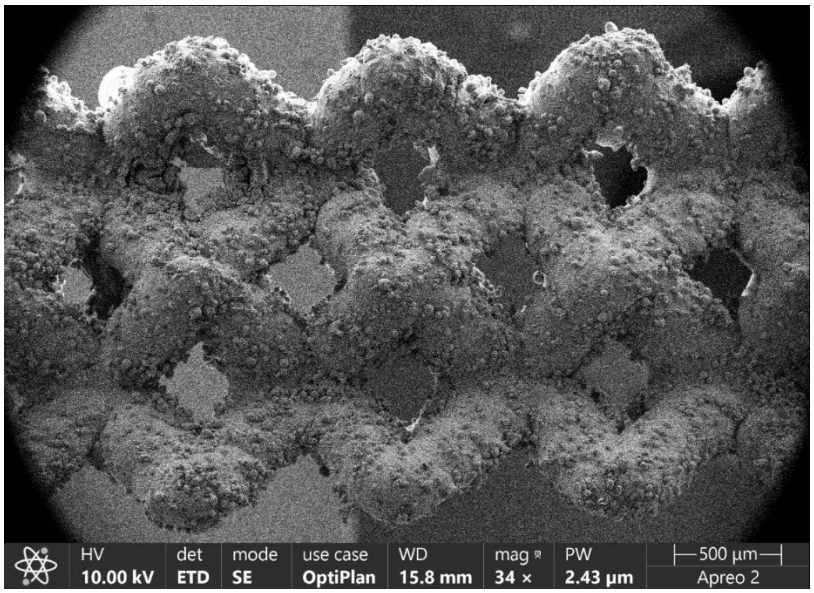

Figure 11. Image of 2 node lattice sample prior to loading in in situ rig

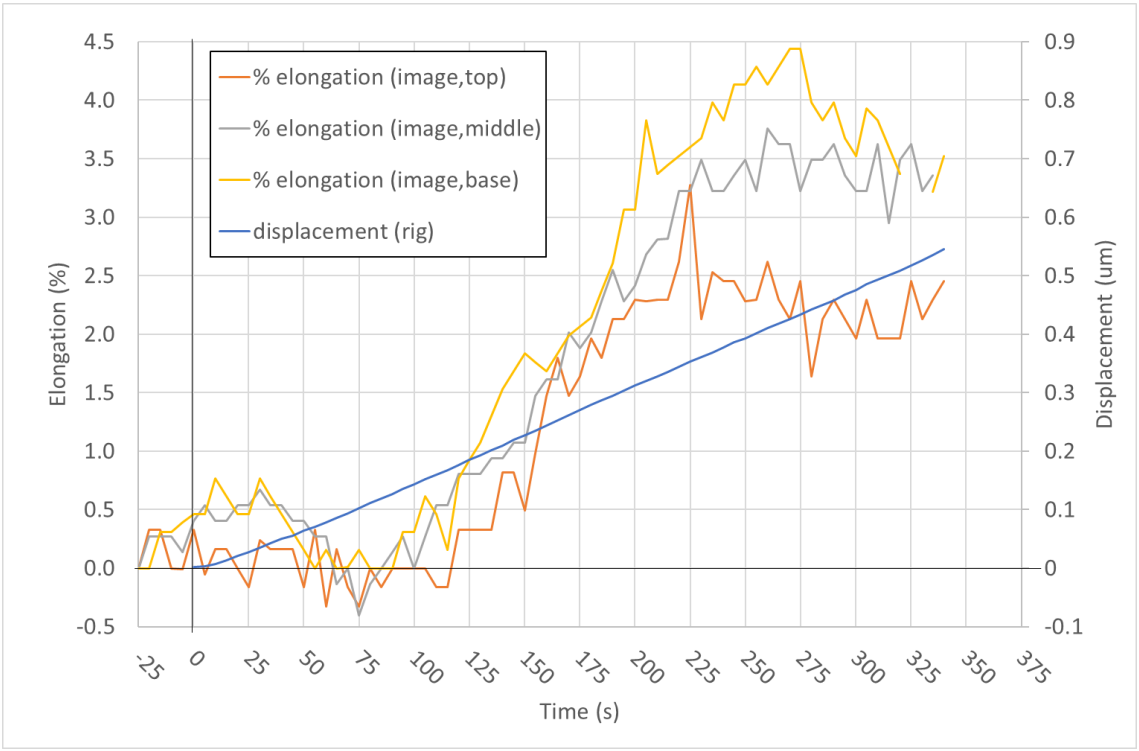

Figure 12: Elongations measured the from image sequence of the loading of the sample in the previous figure. Plotted on the same time base is the displacement measured by the rig.

The difference in the elongation measured at the three positions across the sample also illustrates the usefulness of localised measurement of strain from the SEM images. The smaller

elongation at the top of the image coincides with the region in which failure first occurred with the fracture working through the lattice towards the bottom (of the image) where elongation was greatest. However, the results also illustrate the limitations of imaging: the first fracture started in the ligament hidden beneath the one imaged and so the exact point of initiation cannot be identified by time against the load-displacement data.

If the average elongation of ≈3% was assumed to have occurred across the entire 9 mm length of the lattice structure, then the total displacement would be 270 µm. Adding this to the ≈ 50 µm compliance experienced in reaching the UTS of 66 N at 0.8 µm/N suggests the total displacement measured by the rig should have been 320 µm. Given the possible errors introduced by averaging the elongation over the full sample length and by the uncertainty in correlation of the start times for measurement, this predicted total displacement is in surprisingly good agreement with the 310 µm rig-measured displacement plotted in Figure 10.

3.3 UNCERTAINTY DUE TO SAMPLE MISALIGNMENT

Tensile tests were conducted on five unit-cell ALM samples at a 0.1 mm/min strain rate. The first sample was aligned with the stage loading axis, while the second sample was misaligned by 2°. The forces and displacements recorded during these tests, along with the dimensions of the samples, were used to compute the stress-strain curve (as depicted in Figure 13a). The results showed a slight decrease in the UTS from 46.8 MPa for the aligned sample to 46.6 MPa for the misaligned sample. Despite this minor difference in UTS, the overall stress-strain curve behaviour was comparable for both samples.

In terms of fracture behaviour, the aligned sample exhibited a fracture along the Y-axis, with the fracture on the joints extending from the top to the bottom of the sample cross-section (Figure 13b). On the other hand, the misaligned sample demonstrated a shearing fracture that initiated from the bottom and continued in the shear direction instead of a uniaxial direction (Figure 13c to e).

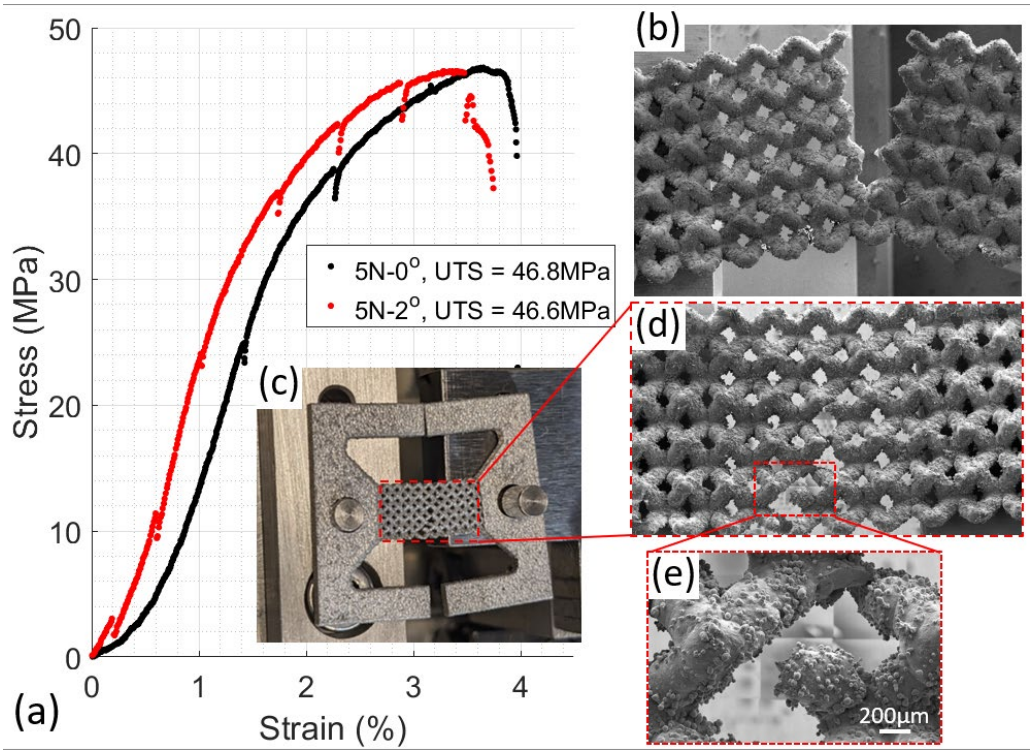

Figure 13: (a) Stress-strain curve of two ALM samples with five unit-cells tested in tension at 0.1 mm/min strain rate, with one being 2° misaligned from the loading axes. (b) Fracture surface of the aligned sample. (c and d) Fracture surface of the misaligned sample, with a (e) zoomed-in area.

The observed behaviour can be attributed to the effects of alignment on the mechanical response of the samples during tensile testing. Proper alignment ensures the load is uniformly distributed across the sample, leading to a uniaxial fracture along the loading direction. Conversely, misalignment can introduce bending moments and offsets that can distort the sample, skew the measurement, and exert force on only a portion of the sample. This can result in a shearing fracture, as observed in the misaligned sample. Furthermore, the slight decrease in UTS for the misaligned sample could be due to the additional bending strain superimposed on the axial strain due to misalignment. However, since the difference in UTS is marginal, it suggests that the material's inherent mechanical properties, such as its yield strength and strain hardening characteristics, play a more significant role in determining its UTS than the effects of alignment, which is consistent with previous quasi-static testing results [4].

Furthermore, differences in the mechanical response between single ligament test pieces tested were initially thought to be due to microstructural. However, further investigation revealed that the offset is likely due to a slight misalignment caused by the sample-building process [5]. Misalignment during tensile testing can significantly influence test results, especially at small strains. This is because misalignment can introduce bending moments and offsets that can distort the sample, skew the measurement, and exert force on only a portion of the sample.

4 CONCLUSION

The report presents a summary of some of the issues involved in determining the uncertainties in the micromechanical testing of fine scale lattice structure ALM samples in the SEM. The primary sources of uncertainty have been reviewed, considering the measurement of sample dimensions and homogeneity, displacement load measurements, and sample misalignment.

One of the key findings relates to displacement measurement, where the study reveals that without load, the stage movement is remarkably consistent. The stage itself is very stiff, but with the loading system employed using only dowels to locate the ALM lattice samples and avoid straining them by clamping, compliance is introduced into the system. This was estimated to be approximately 0.8 μm/N at a strain rate of 0.1 mm/min and 0.2 mm/min.

Regarding load measurement, the precision of the 2 kN load cell, after calibration, showcased an excellent repeatability with a phantom force (preload) identified to be approximately 2.1 ± 1.3 N. Stress-strain curves adjusted for preload forces depicted typical behaviour for AlSi10Mg samples, with those composed of five-unit cells enduring the highest force before fracturing. The stage showed precision/repeatability and accuracy when compared to other machines. However, the precision of load does not translate well to stress because of the difficulties measuring sample dimensions specific to ALM lattice samples.

Misalignment, even as minor as 2°, was shown to alter stress distribution, leading to shearing fractures and although the effect on ultimate tensile strength (UTS) was minimal.

In addition, when conducting mechanical tests on metals, it is important to consider the potential effects of stress relaxation. This phenomenon can influence the material's response to loading and unloading, affect the accuracy of the measurements, and ultimately impact the interpretation of the material's mechanical properties.

5 FUTURE WORK

As mentioned earlier, using full-field methods like digital image correlation can provide an alternative to strain measurement rather than relying on the rig encoder. The use of the DIC technique inside a scanning electron microscope (SEM) to study in-situ the fracture behaviour and other small-scale deformation behaviour was explored in 2003 by Tatschl and Kolednik [12] using speckled copper, and in 2005 by Fonseca *et al.* [13] studied antler bone and etched ferritic steel without applying a speckle pattern (naturally patterned). Subsequently, other researchers [14–16] employed SEM-DIC using an artificial speckle pattern, mainly by depositing nano-size gold particles [17] to take advantage of gold’s high atomic number (brighter appearance, which improves contrast, thus, measurement accuracy).

Since then, the utility of SEM-DIC has grown, but some major sources of error were noted, such as (1) the change of focus during the experiment due to the out-of-plane displacement (especially during plastic deformation); (2) the effect of the stray electric field generated by the mechanical stage on the electron optics; (3) deformation-developed out-of-plane microstructural features (e.g. slip bands) which create a new pattern; this can be mitigated by

using Lithography patterning which is very expensive and time-consuming; (4) single to noise (S/N) ratio which can be alleviated by using FEG-SEM rather than tungsten-SEM and applying a local averaging filter with high beam current and long dwell time which in turn makes image acquisition longer and stress relaxation more pronounced; (5) non-uniform and change in contrast or brightness during the test, and (6) the variety of distortions associated with SEM imaging [18,19].

These distortions can arise from the beam deflection coils, electromagnetic lenses, lens aberrations, sample tilt, etc. It can be grouped into (1) spatial distortion, which is dominant at low magnification (up to 1.6 pixels at 730 nm/pixel resolution) and can be decreased by centring the field-of-view during the test; and (2) drift distortion caused by thermal expansion of different SEM's components, prevalent at high magnification (up to 0.36 pixels/minute at 29 nm/pixel resolution) and not relative to the chamber pressure [18,20].

This is without considering material-specific issues like (1) sample charging, (2) local heating of the specimen due to the electron beam, which is particularly pronounced in materials with low thermal conductivity, (3) strain heterogeneity in materials with complex microstructures like ALM, which may not accurately represent the strain of the bulk or even the other surface of the sample.

Despite these challenges, SEM-DIC is extremely important as it enables the experimental investigation of full-field deformations at much smaller length scales than is possible using optical digital image correlation methods. In addition, by combining SEM-DIC with techniques like electron backscatter diffraction (EBSD) microstructure mapping, it is possible to link in-situ deformation behaviour, at the length scale of the microstructure, directly to the underlying crystallography of the material. Thus, a full investigation of the effect of these aforementioned factors is needed, especially at different temperatures with consideration to the additional impact of aging and stress relaxation that occur during scanning.

APPENDIX: NEWTEC'S UNCERTAINTY IN DISPLACEMENT WITHOUT LOADING

Similar to section 3.1.2, a single leadscrew 5kN NewTec rig was moved to a specific distance without applying load. At the same time, the SEM's field of view was focused on a feature that was imaged before and after the stage, which was displaced by a specific value. The SEM images were acquired using ZESIS Auriga 60 at 5kV and 30 µm aperture size using the secondary electron detector, and Linear Stack Alignment with the SIFT plugin in Fiji (ImageJ) was used to track movement in the 3 sets of images obtained during the test.

As shown in Figure 14, there is a slight discrepancy between the stage's recorded values and those obtained from image registration. The blue 1:1 line in Figure 14 has an R^2 of 0.79, indicating more than 20% inconsistency between the recorded and actual displacement.

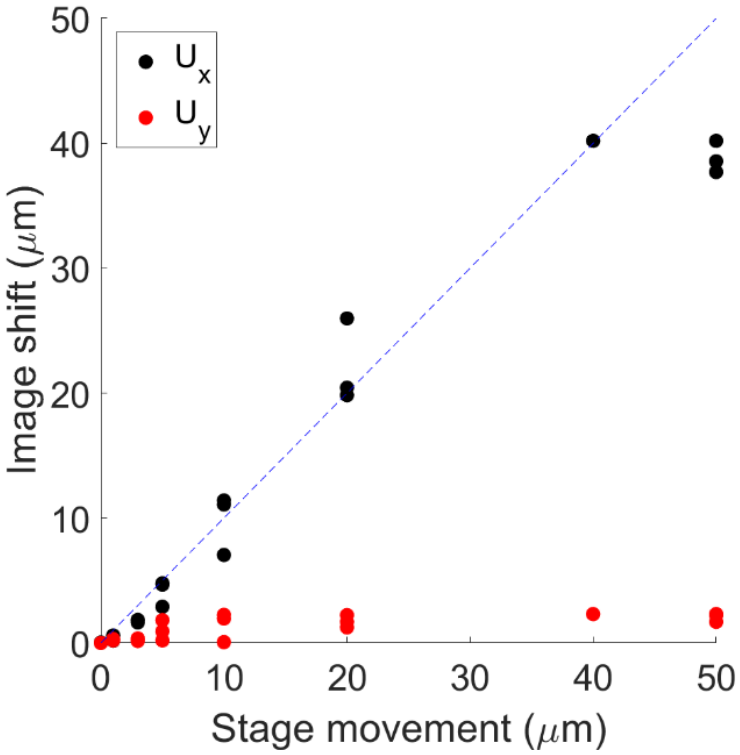

Figure 14: The features in were tracked across the three FOVs, compared to the recorded jaw displacement, and plotted.

6 REFERENCES

[1] National Physical Laboratory Teddington. Manual of codes of practice for the determination of uncertainties in mechanical tests on metallic materials : Project UNCERT, EU Contract SMT4-CT97-2165, Standards Measurement & Testing Programme 2000.

[2] Papirno R, Weiss H. Factors That Affect the Precision of Mechanical Tests. ASTM International100 Barr Harbor Drive, PO Box C700, West Conshohocken, PA 19428-2959; 1989. https://doi.org/10.1520/STP1025-EB.

[3] Basaldella M, Oneschkow N, Lohaus L. Influence of the specimen production and preparation on the compressive strength and the fatigue resistance of HPC and UHPC. Mater Struct 2021;54:99. https://doi.org/10.1617/s11527-021-01696-9.

[4] Fry AT, Lodeiro MJ, Koko A, Booth-Downs F, Crocker LE. Effect of specimen misalignment in static and fatigue testing of small-scale test pieces. Teddington, UK: 2023. https://doi.org/10.47120/npl.MAT122.

[5] Fry AT, Crocker LE, Lodeiro MJ, Poole M, Woolliams P, Koko A, et al. Tensile property measurement of lattice structures. Teddington, UK: 2023. https://doi.org/10.47120/npl.MAT119.

[6] Fry AT, Crocker LE, Woolliams P, Poole M, Koko A, Breheny C. Tensile Property Measurement of AlSi10Mg Lattice Structures - From Single Strut to Lattice Networks. Advances in Materials, Manufacturing, and Repair for Power Plants: Proceedings from the Tenth International Conference, Bonita Springs Florida, USA: ASM International; 2024, p. 207–18. https://doi.org/10.31399/asm.cp.am-epri-2024p0207.

[7] Lowe DG. Distinctive Image Features from Scale-Invariant Keypoints. Int J Comput Vis 2004;60:91–110. https://doi.org/10.1023/B:VISI.0000029664.99615.94.

[8] Rohaizat NI, Alharbi K, Pinna C, Ghadbeigi H, Hanlon DN, Azid IA. Using a Correction Factor to Remove Machine Compliance in a Tensile Test on DP1000 Steel Validated

with 2D Digital Image Correlation Technique. Advanced Structured Materials 2021;148:113–23. https://doi.org/10.1007/978-3-030-67750-3_10/COVER.

[9] Hariharan K, Majidi O, Kim C, Lee MG, Barlat F. Stress relaxation and its effect on tensile deformation of steels. Materials & Design (1980-2015) 2013;52:284–8. https://doi.org/10.1016/J.MATDES.2013.05.088.

[10] Li Y, Shi Z. A New Method to Characterize and Model Stress-Relaxation Aging Behavior of Aluminum Alloys Under Age Forming Conditions. Metall Mater Trans A Phys Metall Mater Sci 2022;53:1345–60. https://doi.org/10.1007/S11661-022-06594-5/FIGURES/17.

[11] Zheng JH, Jin Y, Xu L, Fan C, Song W, Chen Y. Comparative Study of Creep and Stress Relaxation Behaviour during Ageing of 7050 Aluminum Alloy. Metals 2023, Vol 13, Page 778 2023;13:778. https://doi.org/10.3390/MET13040778.

[12] Tatschl A, Kolednik O. A new tool for the experimental characterization of micro-plasticity. Materials Science and Engineering: A 2003;339:265–80. https://doi.org/10.1016/S0921-5093(02)00111-9.

[13] Fonseca Q Da, Mummery PM, Withers PJ. Full-field strain mapping by optical correlation of micrographs acquired during deformation. J Microsc 2005;218:9–21. https://doi.org/10.1111/j.1365-2818.2005.01461.x.

[14] Sutton MA, Li N, Joy DC, Reynolds AP, Li X. Scanning Electron Microscopy for Quantitative Small and Large Deformation Measurements Part I: SEM Imaging at Magnifications from 200 to 10,000. Exp Mech 2007;47:775–87. https://doi.org/10.1007/s11340-007-9042-z.

[15] Héripré E, Dexet M, Crépin J, Gélébart L, Roos A, Bornert M, et al. Coupling between experimental measurements and polycrystal finite element calculations for micromechanical study of metallic materials. Int J Plast 2007;23:1512–39. https://doi.org/10.1016/J.IJPLAS.2007.01.009.

[16] Kovac J, Alaux C, Marrow TJ, Govekar E, Legat A. Correlations of electrochemical noise, acoustic emission and complementary monitoring techniques during intergranular stress-corrosion cracking of austenitic stainless steel. Corros Sci 2010;52:2015–25. https://doi.org/10.1016/J.CORSCI.2010.02.035.

[17] Di Gioacchino F, Quinta da Fonseca J. Plastic Strain Mapping with Sub-micron Resolution Using Digital Image Correlation. Exp Mech 2013;53:743–54. https://doi.org/10.1007/s11340-012-9685-2.

[18] Kammers AD, Daly S. Digital Image Correlation under Scanning Electron Microscopy: Methodology and Validation. Exp Mech 2013;53:1743–61. https://doi.org/10.1007/s11340-013-9782-x.

[19] Maraghechi S, Hoefnagels JPM, Peerlings RHJ, Rokoš O, Geers MGD. Correction of Scanning Electron Microscope Imaging Artifacts in a Novel Digital Image Correlation Framework. Exp Mech 2019;59:489–516. https://doi.org/10.1007/S11340-018-00469-W/FIGURES/21.

[20] Mello AW, Book TA, Nicolas A, Otto SE, Gilpin CJ, Sangid MD. Distortion Correction Protocol for Digital Image Correlation after Scanning Electron Microscopy: Emphasis on Long Duration and Ex-Situ Experiments. Exp Mech 2017;57:1395–409. https://doi.org/10.1007/s11340-017-0303-1.